

Research Article

Numerical Simulation of Fluctuating Wind Effects on an Offshore Deck Structure

Jin Ma,¹ Dai Zhou,^{1,2,3} Zhaolong Han,¹ Kai Zhang,^{1,4} Jennifer Nguyen,⁵ Jiabao Lu,¹ and Yan Bao¹

¹School of Naval Architecture, Ocean and Civil Engineering, Shanghai Jiao Tong University, Shanghai 200240, China

²Collaborative Innovation Center for Advanced Ship and Deep-Sea Exploration (CISSE), Shanghai 200240, China

³State Key Laboratory of Ocean Engineering, Shanghai Jiao Tong University, No. 800, Dongchuan Road, Shanghai 200240, China

⁴Department of Civil Engineering, Graduate School of Urban Innovation, Yokohama National University, Yokohama 2408501, Japan

⁵Cullen College of Engineering, University of Houston, Houston, TX 77004, USA

Correspondence should be addressed to Dai Zhou; zhoudai@sjtu.edu.cn

Received 5 November 2016; Revised 2 February 2017; Accepted 28 February 2017; Published 30 March 2017

Academic Editor: Marco Belloli

Copyright © 2017 Jin Ma et al. This is an open access article distributed under the Creative Commons Attribution License, which permits unrestricted use, distribution, and reproduction in any medium, provided the original work is properly cited.

The offshore structures that play a vital role in oil and gas extraction are always under complicated environmental conditions such as the random wind loads. The structural dynamic response under the harsh wind is still an important issue for the safety and reliable design of offshore structures. This study conducts an investigation to analyze the wind-induced structural response of a typical offshore deck structure. An accurate and efficient mixture simulation method is developed to simulate the fluctuating wind speed, which is then introduced as the boundary condition into numerical wind tunnel tests. Large eddy simulation (LES) is utilized to obtain the time series of wind pressures on the structural surfaces and to determine the worst working condition. Finally, the wind-induced structural responses are calculated by ANSYS Parametric Design Language (APDL). The numerically predicted wind pressures are found to be consistent with the existing experimental data, demonstrating the feasibility of the proposed methods. The wind-induced displacements have the certain periodicity and change steadily. The stresses at the top of the derrick and connections between deck and derrick are relatively larger. These methods as well as the numerical examples are expected to provide references for the wind-resistant design of the offshore structures.

1. Introduction

Numerous offshore structures have been constructed to supply oil and gas all over the world in recent years. The offshore structures are designed for resisting random wind and wave loads. In the current design experience, the lateral random wind load in the design of fixed offshore structures is of order of 10% in the total lateral design loads and 25% in the case of floating platforms [1, 2]. Many accidents involving deck components such as a derrick and crane due to the random wind loads have already been reported in damage investigation [3]. However, practical estimation and assessment of the fluctuating wind and wind-induced dynamic response of the complex offshore deck structures are still involved problems [4]. Therefore, with the development of the oil exploitation to deep sea, it is necessary and important

to carry out the wind field analyses of offshore structures to guarantee a reasonable safety design.

In general, the wind-induced structural responses are numerically investigated by applying wind pressures on the structural surfaces by the time-domain analysis method [5, 6]. Meanwhile, the numerical simulation in the present study could override the two-way fluid-structure interaction with the wind-induced structural response with small deformation [7]. Wind pressures on structures could be extracted by the full-scale measurement, wind tunnel test, and computational fluid dynamics (CFD) methods. Each of these methods is complementary with another in view of their own advantages and limitations [8]. The full-scale measurement can record the firsthand data of wind pressures on prototype structures. However, it is generally conducted with the limitations of several objective conditions such as

weather conditions, high cost, and site conditions [9]. Wind tunnel test is a relatively mature and effective technique in wind engineering on scaled models of complex structures [10, 11]. However, there are also several limitations in wind tunnel tests for accurate investigations of wind pressures on structures as follows: (1) Reynolds numbers of scaled model tests are smaller than those of prototype structures; (2) the wind field conditions can hardly be reproduced exactly in wind tunnel tests [10].

Owing to the rapid developments of computer power and computational methods, CFD predictions have been widely used to analyze the wind flows around prototype structures in engineering practice [12]. Large eddy simulation (LES), as one of the main CFD methods, has been widely applied in the simulations of wind fields. With powerful CFD tools such as LES, it is possible to conduct full-scale size simulations of prototype structures in high Reynolds numbers flows and provide abundant detailed data and information, such as pressure distributions on structural surfaces [13].

It is understood that proper generation of the inlet boundary conditions for CFD simulations, especially for LES in computational wind engineering (CWE), is essential in the analyses of wind pressure distributions and the dynamic responses of prototype structures [14]. Therefore, the improvement of simulating fluctuating wind speed in the inlet boundary is provided in the present study. Combining with the advantages of weighted amplitude wave superposition (WAWS) [15] and autoregression (AR) [16, 17] methods with high accuracy and less time cost, respectively, a mixture simulation (MS) method is proposed and demonstrated as an efficient and accurate simulation method in the present work.

In summary, the main objective of this present study is to conduct wind field analyses of the offshore deck structures which are carried out by a joint application of CFD technique and structural finite element analysis. Furthermore, time series of wind pressures on the structural surfaces at different wind directions and inclined angles of the platform are extracted in CFD wind tunnel tests and then applied to the finite element model to investigate the wind-induced structural response.

This paper is organized as follows: the structural models in numerical simulation and wind tunnel test are presented in Section 2. Methods for conducting CFD predictions are provided in Section 3. An accurate and efficient MS method for simulating fluctuating wind speed as boundary conditions is proposed in Section 4. Computational procedures for the whole wind field analyses of the offshore deck structures are included in Section 5. The validation tests for the MS and LES methods and numerical cases of wind field investigations are carried out in Section 6.

2. The Model Semisubmersible Platform

The semisubmersible platform in this study is the 6th-generation deepwater drilling platform, shown in Figure 1(a), and possesses the function of intelligent drilling technology attaining the advanced level all over the world. The major structural components of this platform include derrick, deck,

TABLE 1: The size parameters of the semisubmersible platform.

Members	Dimensions (length × width × height)/m
The lower part of derrick	17 × 17 × 42
The upper part of derrick (wedge)	17 × 17 × 22
Deck	74.42 × 74.42 × 8.6
Column	17.39 × 17.39 × 21.46

columns, and floating bodies. The main parameters of this platform are listed in Table 1.

The tested model in Figure 1(b) was scaled as 1:100 in [18]. The full-scale CFD numerical model of this platform in the present CFD simulations is built based on the tested scaled model [18] and numerical full-scale model [19]. In view of the major consideration of wind field analyses, the offshore platform structures under the water are hidden and the derrick is totally enclosed as shown in Figure 1(c) which is demonstrated that the extracted wind pressures are applicable in the wind-induced dynamic response analyses [19, 20]. However, the structural computational model of the derrick in the following time-domain analysis is similar to a real structure and not enclosed, as is plotted in Figure 1(d).

One thing to note is that two types of numerical models, the CFD numerical model and the structural computational model, are applied in this present study. The CFD numerical model is a platform model used for LES simulations, which is established by using a combination of Rhino (Robert McNeel & Assoc, USA) and ICEM CFD (ANSYS, Inc., USA). The structural computational model is a finite element model of this platform for structural dynamic response analyses in time domain, which is built by ANSYS Parametric Design Language (APDL) (ANSYS, Inc., USA). The finite elements of the local components are listed as follows: the derrick adopts beam element, the deck uses shell element, and the columns adopt solid element.

3. Numerical Simulation

In this section, together with the commercial CFD software Fluent 14.5 (ANSYS, Inc., USA), the unsteady-state analysis of the LES approach is used to predict the time series of wind pressures on the surfaces of structures above the water surface at different working conditions. Fluent 14.5 conducts LES simulations based on finite volume method (FVM) [23]. Then, the wind-induced structural responses are explored by the extracted wind pressures acting on the structures using APDL and time-domain analysis method cooperatively [24]. The detailed computational algorithms and treatments of wind field analyses are addressed in the following subsections.

3.1. CFD Predictions

3.1.1. LES Turbulence Model. In the present LES study, LES separates flow motions into large and small eddies which is calculated by using a combination of the direct simulation

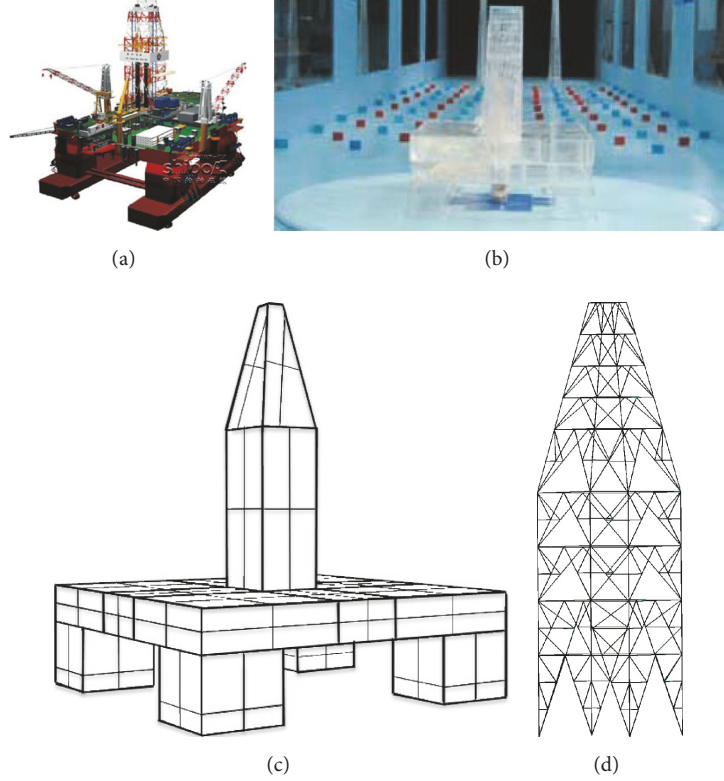


FIGURE 1: (a) The practical semisubmersible platform. (b) The tested model of wind tunnel tests [17]. (c) The numerical model used in CFD wind tunnel predictions. (d) The derrick model for wind-induced analyses.

method and general model theory [25]. In view of these studies in the LES simulations whose proposed methods are applied for full-scale CFD numerical model under Reynolds number greater than 10^8 [10], these methods are adopted to carry out the present LES simulations under Reynolds number of approximately 6×10^7 . It is worth mentioning that these methods, such as one-equation model, are suitable for relatively coarse grid case and high Reynolds number flows [26]. The accuracy and reliability of the proposed numerical framework have been validated by the consensus between numerical and experimental results in the previous studies [10, 26].

The governing equations of an incompressible flow for LES simulations [26] are expressed as

$$\begin{aligned} \frac{\partial \rho \bar{v}_i}{\partial t} + \frac{\partial \rho \bar{v}_i \bar{v}_j}{\partial x_j} &= -\frac{\partial}{\partial x_i} \left(\bar{P} + \frac{2}{3} \rho k_{sgs} \right) \\ &+ \frac{\partial}{\partial x_i} \left[2\rho (v_s + v) \bar{S}_{ij} \right], \end{aligned} \quad (1)$$

$$\frac{\partial \bar{v}_i}{\partial x_i} = 0,$$

where \bar{v}_i is the large-scale wind velocity field tensor, \bar{P} the resolved pressure, \bar{S}_{ij} the resolved strain-rate tensor, ρ the air density, v the kinematic viscosity, k_{sgs} the subgrid scale (SGS) kinematic energy, v_s the SGS eddy viscosity, and

$$\begin{aligned} v_s &= C_v \Delta_v \sqrt{k_{sgs}}, \\ \Delta_v &= \frac{\bar{\Delta}}{1 + C_k \left(\frac{\bar{\Delta}^2 \bar{S}^2}{k_{sgs}} \right)}, \\ \frac{\partial k_{sgs}}{\partial t} + \frac{\partial \bar{v}_j k_{sgs}}{\partial x_j} &= -\tau_{ij} \bar{S}_{ij} - C_\epsilon \frac{k_{sgs}^{3/2}}{\bar{\Delta}} \\ &+ \frac{\partial}{\partial x_j} \left[\left(C_d \Delta_v \sqrt{k_{sgs}} + v \right) \frac{\partial k_{sgs}}{\partial x_j} \right] \\ &- 2v \frac{\partial k_{sgs}}{\partial x_i} \frac{\partial k_{sgs}}{\partial x_j}, \end{aligned} \quad (2)$$

where C_v , C_k , C_ϵ , and C_d are the constant [27, 28] and $\bar{\Delta}$ is the length scale of filter and can be determined according to Huang and Li's work [26].

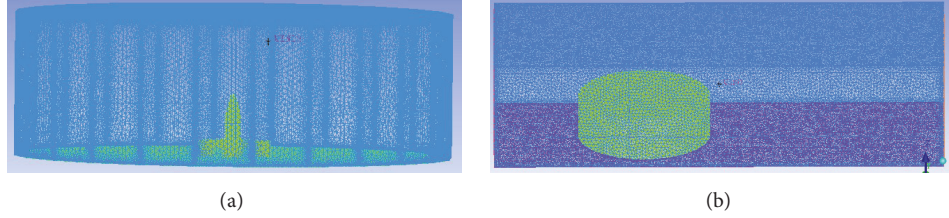


FIGURE 2: The meshing results: (a) Block 1; (b) Block 2.

The improved LES approach proposed by Huang and Li [26] has been developed as a Fluent User Defined Function (UDF) library, which has been applied in conducting LES simulations of tall buildings and long-span complex roof structures in the previous studies [10, 12].

3.1.2. Numerical Algorithms. In the LES predictions, all the discrete equations are solved by the pressure implicit with splitting of operators (PISO) method. The time and spatial discretization are both treated by second-order discrete schemes. Bounded central differencing is adopted for momentum discretization. The LES simulations are performed together with ANSYS/Fluent 14.5 and the parallel calculations of 16 central processing units. The total time steps are nearly 41000 with 0.05 s per time step, which are sufficient to reach the statistical convergence for LES simulations [10, 12].

3.1.3. Computational Domain and Mesh Arrangement. The numerical model of this offshore platform is established in full-scale sizes, as sketched in Figure 1(c). The dimensions of the computational domain, sketched in Figure 2, are 2600 m (L_x) \times 600 m (L_y) \times 200 m (L_z) as the computational domain is 35 (L_x) \times 8 (L_y) \times 2.5 (L_z) [11]. The blocking rate of CFD numerical model in the computational domain is less than 3%, which is generally acceptable in CWE [9]. According to the multiblock technique in the previous study [12], the flow field consists of two blocks: The small cylindrical flow field and CFD numerical model, which are combined together by a Boolean operation, are defined as “Block 1” in Figure 2(a), and the remaining part (i.e., the big rectangular flow field) is defined as “Block 2” in Figure 2(b). One thing is to note that the CFD numerical model is nested in “Block 1.” Rotating “Block 1” the specified angle immediately can carry out LES simulations at the specified wind direction, by which LES simulations can be conducted at multiple wind directions conveniently. Numerous tetrahedral grids are generated in the neighborhood of the structural surfaces, especially in the vicinity of the derrick, and the grid stretching ratio is kept to be <1.05 . The maximum and minimum grid lengths in the neighborhood of the structural surfaces are 0.8 m and 0.2 m, respectively. Hexahedron grids are adopted in the regions far away from the calculating model and the grid stretching ratio is relatively enlarged for reducing the total mesh number for the sake of saving time cost in computation. In view of

the computer performance, computing time, and engineering requirements, the minimum, maximum, and mean values of y^+ are 2.53308, 4.89245, and 3.48798, respectively. According to the previous study [29], although a recommended value for y^+ is about 1, values lower than 5 are acceptable because the cell stays in the viscous sublayer.

The total mesh number is nearly 11 million. According to LES theory, the mesh quantity should reach $Re^{9/4}$ in order to provide very accurate numerical results. And the more the mesh elements in the fluid domain, the higher the computational accuracy that will be reached. However, it requires much more computing time cost and higher computer performance which would be a heavy task for CFD simulation. In order to make it feasible to reach moderate accuracy while simultaneously satisfying the engineering requirement (which can allow 10~30% error for structure safety design), the grid resolution has to be reduced. For obtaining relative accuracies of the wind pressures, forces, and comparing wind coefficients, we conducted a grid resolution test in the following validation test and found that the presented mesh balances time cost and numerical accuracy, satisfying the engineering requirements.

3.1.4. Boundary Conditions. The boundary conditions are described as the wind velocity profile in accordance with an exponential rule, which can satisfy the Navier-Stokes equations in LES simulations [10, 18]:

$$V_z = V_0 \left(\frac{H}{H_0} \right)^\alpha, \quad (3)$$

where V_z and V_0 are the average wind velocities at the height of H and H_0 and α is related to geomorphologic features [22].

In unsteady-state analysis of the LES simulations, the Fluent code provides a direct and convenient method to generate a time-dependent turbulent fluctuating wind velocity field. However, it is reported that the generated wind field by the Fluent code decays rapidly in the inertial range and is not well approximated as the marine random wind [26]. The power spectral density (PSD) of the fluctuating wind is fitted by NPD (Norwegian Petroleum Directorate) spectrum in the present study [22]:

$$S(f) = \frac{320 (V_0/10)^2 (z/10)^{0.45}}{(1 + 1.5F)^{3.56}}, \quad (4)$$

$$F = 172f \left(\frac{z}{10} \right)^{2/3} \left(\frac{V_0}{10} \right)^{-3/4},$$

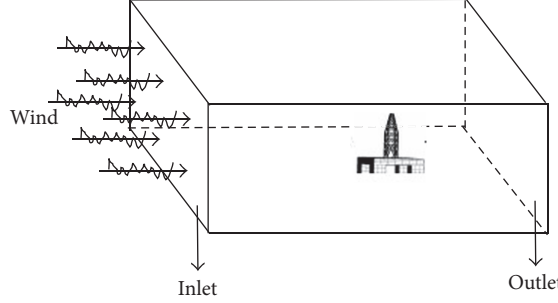


FIGURE 3: The sketch of the inlet boundary of the fluctuating wind.

where $S(f)$ is the PSD function, f the wind frequency, V_0 the average wind speed at the height of H_0 , and z the height above sea level.

Given a clear explanation of the wind characteristics, the fluctuating wind speed of the inlet boundary shown in Figure 3 is simulated by the MS method proposed in the following section. This new simulation method, MS method, can generate the time series of wind velocities of a number of spatial nodes accurately and efficiently. The pressure fluctuation on structural surfaces can be solved by importing the inlet boundary conditions in LES simulations in the commercial software ANSYS/Fluent 14.5. Therefore, velocity and pressure components together satisfy the Navier-Stokes equations.

In order to guarantee the convergence property and efficiency in LES simulations, the fluctuating wind velocities at each time step at the inlet are modified through the equal total flow of the inlet and outlet on the basis of the previous studies [20, 30]. The equation is described as

$$v_{i+1} = v_i - \frac{(\sum_{i=1}^n v_i A_i - \Omega)}{A}, \quad (5)$$

where v_i is the fluctuating wind speed at time step i , A_i the area of the corresponding grid cell, A the total area of the inlet boundary, and Ω the total flow of the outlet boundary at the corresponding time step.

According to the work of Lu et al. [20] and Shirani et al. [30], the wind velocities at each time step being read and updated in Fluent 14.5 are found to be slightly smaller than the initial wind velocities generated by the self-made MATLAB program.

3.1.5. Data Analyses. The analyses of wind pressure distribution are carried out in terms of nondimensional coefficients, C_p and C_{prms} , of a measuring point i defined, respectively, as

$$\begin{aligned} C_p &= \frac{\bar{P}_i}{0.5\rho V_0^2}, \\ C_{prms} &= \frac{P_{i,rms}}{0.5\rho V_0^2}, \end{aligned} \quad (6)$$

where C_p and C_{prms} are the mean and RMS pressure coefficients, respectively, \bar{P}_i is the mean pressure, $P_{i,rms}$ is the RMS

pressure, ρ is the air density, and V_0 is the average of wind speed at the height of 10.0 m.

According to China Classification Society common rules and [19], the equation of the shape coefficient of a structural member is expressed as

$$\begin{aligned} sc_i &= C_p \left(\frac{160}{z} \right)^{0.2}, \\ SC &= \frac{\sum_i sc_i SA_i}{SA}, \end{aligned} \quad (7)$$

where i is a measuring point on a specified structural member, sc_i is the shape coefficient i , C_p the mean pressure coefficient, z the height of a measuring point i , SA_i the area of the structural surface which a measuring point i belongs to, and SA the total area of multiple structural surfaces. The average pressure coefficients, SC , are changing with the wind directions. Therefore, the shape coefficients vary with wind directions.

3.2. Wind-Induced Structural Response Analyses. The time series of the extracted wind pressures are applied to the offshore structures and the wind-induced dynamic responses are calculated by time-domain analysis method together with APDL solving the structural dynamic equation as follows:

$$[M] \{ \ddot{u} \} + [C] \{ \dot{u} \} + [K] \{ u \} = [F], \quad (8)$$

where $[M]$, $[C]$, and $[K]$ are, respectively, structural mass, damping, and stiffness matrices, $\{ \ddot{u} \}$, $\{ \dot{u} \}$, and $\{ u \}$ are, respectively, acceleration, velocity, and displacement vectors, and $[F]$ are fluctuating wind loads. Meanwhile, (4) is solved by the Newmark- β approach in this present study [22].

In structural dynamic response analysis, the damping matrix $[C]$ is determined by the following equations:

$$\begin{aligned} [C] &= \alpha [M] + \beta [K], \\ \xi_i &= \frac{\alpha}{2\omega_i} + \frac{\beta\omega_i}{2}, \end{aligned} \quad (9)$$

where α and β are the constants in Rayleigh damping which are calculated by the damping ratio in each mode shape ξ_i [20] which is assumed as a constant over a range of frequencies. And ω_i is the structural frequency in each mode shape.

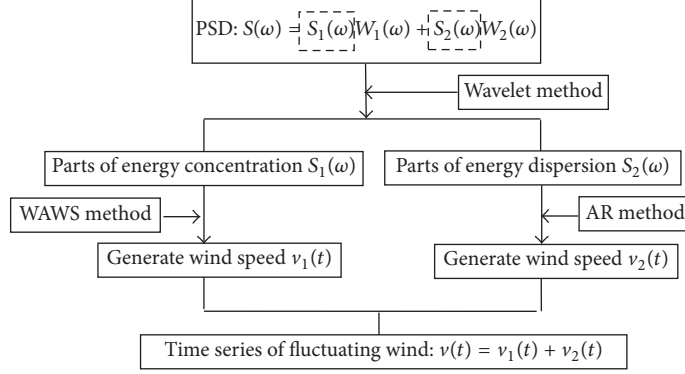


FIGURE 4: The flowchart for simulating the fluctuating using MS method.

4. The Method for Simulating Fluctuating Wind

A mixture simulation (MS) method is proposed to generate the fluctuating wind speed as the boundary conditions in CFD predictions, combining with the weighted amplitude wave superposition (WAWS) method [15] and autoregression (AR) methods [16, 17]. The new approach overcomes the defects of the abovementioned traditional methods and inherits their own advantages which guarantee the computing accuracy and efficiency simultaneously.

Assuming that the fluctuating wind is a stationary stochastic Gaussian process, the stochastic characteristics can be described by the power spectral density (PSD) function [31]. Then, the energy distributions of the PSD function of the fluctuating wind are explored by the wavelet method [32] adopting the Hanning windows [33]. Therefore, the main thoughts of the MS method are listed as follows: the parts of the energy concentration are simulated by the WAWS method [15] and the parts of the energy dispersion are generated by the AR method [16]. The final simulating results of the fluctuating wind are obtained by the superposition of the simulating results by the two methods. The schematic simulation process is concluded in Figure 4. The equation of the calculating process by the MS method is described as follows:

$$S(f) = S_1(f)W_1(f) + S_2(f)W_2(f), \quad (10)$$

where $S(f)$ is the PSD function, f is the wind frequency, $W_1(f)$ and $W_2(f)$ are, respectively, the Hanning windows of the energy concentration and dispersion, and $S_1(f)$ and $S_2(f)$ are, respectively, simulated by the WAWS method and AR method.

The Hanning window number is determined by the energy distribution of the PSD function in the wind field. According to our experience, the window number using the WAWS method is three times larger than it using the AR method. In this way, the MS method could reduce the time cost in computation with no accuracy lost to simulate a kind of loads with the random properties, which is demonstrated in the following validation tests in Section 6.1.

The application of the WAWS and AR methods is briefly presented in the following formula derivation, which has fully considered temporal and spatial correlation in the self-compiled programs.

(1) *The WAWS Method in the MS Method.* Using the WAWS method, the correlation function R_{jm} is expressed as

$$\begin{aligned} R_{jm}(\tau) &= E(v_j(t)v_m(t+\tau)) \\ &= \Delta f \sum_{k=1}^j \sum_{l=1}^N |H_{jk}(f_{kl})| |H_{mk}(f_{kl})| \\ &\quad \cdot \cos(2\pi f_{kl} + \theta_{jk}(f_{kl}) - \theta_{mk}(f_{kl})), \end{aligned} \quad (11)$$

where E is expectation, v is the time series of wind speed, H is obtained by Cholesky decomposition, and $\theta_{jk}(f_{kl})$ is the phase angle between spatial nodes i and j .

Assuming that $N \rightarrow \infty$ and $\Delta f \rightarrow 0$,

$$\begin{aligned} R_{jm}(\tau) &= \int_{s_{l_1}}^{s_{l_1}} \sum_{k=1}^j |H_{jk}(f_k)| |H_{mk}(f_k)| \\ &\quad \cdot \cos(2\pi f_k + \theta_{jk}(f_k) - \theta_{mk}(f_k)) df. \end{aligned} \quad (12)$$

The correlation function is transformed from time domain to frequency domain on the basis of convolution theorem:

$$\begin{aligned} R_{jm}(\tau) \otimes W_1(t) &= \int_{s_{l_1}}^{s_{l_1}} \sum_{k=1}^j |H_{jk}(f_k)| |H_{mk}(f_k)| \\ &\quad \cdot \widehat{W}_1(f) \cos(2\pi f_k + \theta_{jk}(f_k) - \theta_{mk}(f_k)) df \\ &= \int_{s_{l_1}}^{s_{l_1}} \sum_{k=1}^j S_{jk}(f) \cdot \widehat{W}_1(f) \cos(2\pi f_k) df, \end{aligned} \quad (13)$$

where \otimes represents convolution operation.

Time series of wind speed simulated by the WAWS method $v_1(t)$ is obtained by

$$\begin{aligned} v_1(t) &= \sqrt{2\Delta f} \sum_{k=1}^j \sum_{l=1}^N |H_{jk}(f_l)| \cos(2\pi f_l t + \theta_{jk}(f_l) + \varphi_{kl}), \quad (14) \\ &\quad j = 1, \dots, m, \end{aligned}$$

where φ is a random number from 0 to 2π .

(2) *The AR Method in the MS Method.* Similarly, the correlation function in the AR method can be expressed as

$$R_{ij}(\tau) = \int_{s_{l_2}}^{s_{l_2}} S_{ij}(f) \widehat{W}_2(f) \cos(2\pi f \cdot \tau) df, \quad (15)$$

where R is the correlation function.

Time series of wind speed simulated by the AR method $v_2(t)$ is calculated by

$$v_2(t) = - \sum_{i=1}^j \sum_{k=1}^p a_{ijk} v_i(t - k \cdot \Delta t) + u(n), \quad (16)$$

where Δt is the total simulating time step, a the coefficient of autoregression matrix, $u(n)$ the excited white noise through all-zeros filter, and p the order of AR model.

Overall, the total wind speed is obtained by $v(t) = v_1(t) + v_2(t)$, which is shown in Figure 4.

5. The Procedure for the Wind Field Analyses of the Platform

In this section, the details for conducting LES predictions and wind-induced dynamic responses analyses of the deck structures under the action of the fluctuating wind are summarized as follows.

Step 1. Establish the geometric and finite element models by VC++ and APDL.

Step 2. Generate the fluctuating wind speed.

Step 2.1. Simulate and correct the time series of the wind speed by using the MATLAB (MathWorks, USA) self-compiled programs.

Step 2.2. Convert these data into data files in the format that has a .txt extension format. These data files are read by ANSYS/Fluent using the User Defined Functions (UDF) program.

Step 3. Construct the CFD numerical wind tunnel.

Step 3.1. Create the calculation model and mesh files by Rhino and ICEM CFD.

Step 3.2. Set the initial and boundary conditions in ANSYS/Fluent and start the calculation.

Step 3.3. Calculate the resultant forces to determine the worst operating condition.

Step 3.4. Extract the time series of wind pressure on the structural surfaces by the UDF program for the following dynamic response analyses.

Step 4. Carry out the wind-induced dynamic response analyses by APDL.

Step 4.1. Import the finite element model of the platform and deck structures.

Step 4.2. Set the initial and boundary conditions and start the calculation by the Newmark- β method in time domain using the secondary development application programs.

Step 4.3. Extract the calculation results such as the deformations and stresses of nodes and members.

6. Results and Discussion

6.1. Validation Tests. In this subsection, the numerical results are compared to verify that the methods and self-made programs mentioned in Sections 3 and 4 are applicable and effective in the following numerical examples.

6.1.1. Validation for the MS Method. Tests are constructed to demonstrate the accuracy and efficiency of the MS method compared to the traditional simulation methods: the WAWS and AR methods. The time series of the wind speed at any spatial point is simulated by the MS, WAWS, and AR methods, respectively. The comparison between the simulated and theoretical results could determine the best simulation method.

(1) Validation for the Accuracy of the MS Method. The fluctuating wind speed at one single spatial point is simulated by the MS, WAWS, and AR methods, respectively, in the same initial condition listed as follows: the average wind velocity $V_0 = 31.654$ m/s, the number of the sampling points $n = 1200$, time step $\Delta t = 0.1$ s, and the measuring point (in meters) is located at $(0, 0, 5)$. The error between the energy [34] of the simulated and theoretical results solved by (17) can assess the accuracy of the simulation method by fast Fourier transform (FFT) [35] and frequency-time conversion methods [36, 37]:

$$\Omega = \frac{\|X(j\omega)\|^2}{T} = \frac{\left\| \int x(t) e^{-i\omega t} dt \right\|^2}{T}, \quad (17)$$

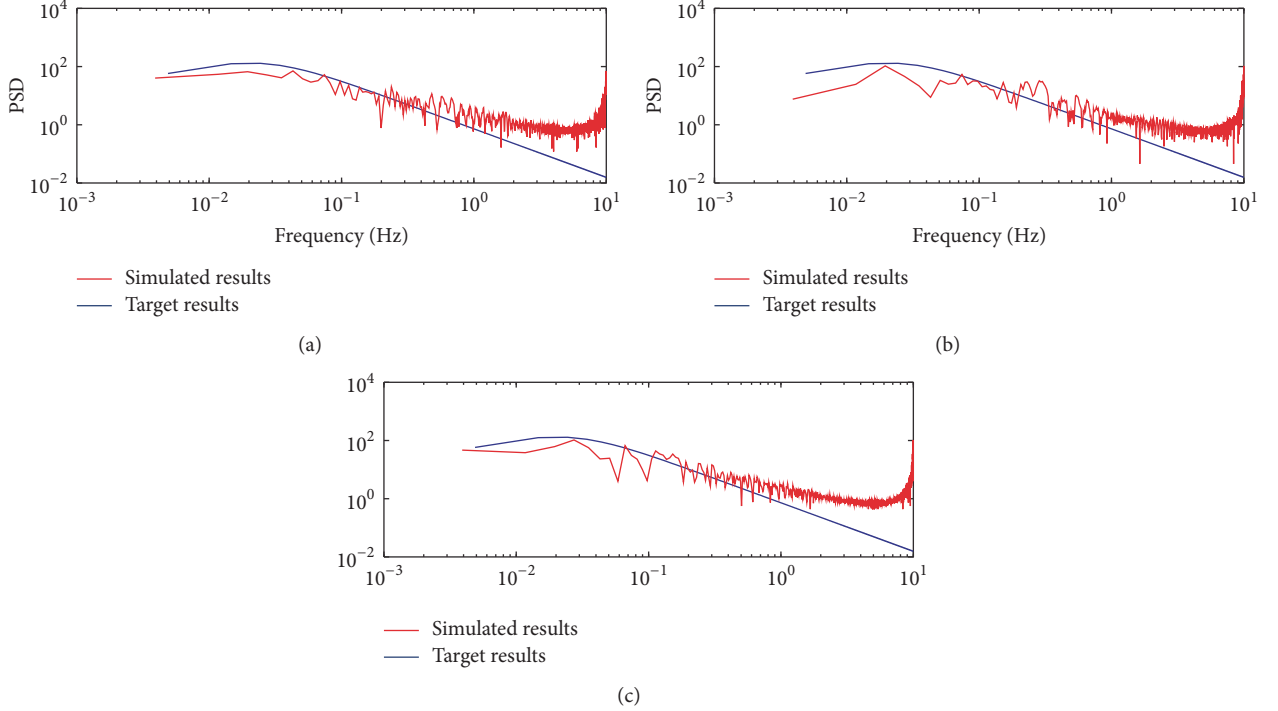


FIGURE 5: The comparison between simulated and target results by MS, AR, and WAWS methods: (a) MS method; (b) AR method; (c) WAWS method.

TABLE 2: The comparison of calculating accuracy between the results of simulated PSD and theoretical PSD.

	MS method	WAWS method	AR method
Theoretical energy	12.6923	12.6923	12.6923
Simulating energy	12.3927	13.6073	14.2073
Error	2.36%	7.21%	11.94%

where $x(t)$ is time series of wind velocity, $X(j\omega)$ the amplitude spectrum obtained from $x(t)$ by FFT, and T the lasting time of time series of wind speed. The energy Ω is calculated by the square of the amplitude spectral mode divided by the lasting time T .

The comparisons between simulated and target results by the MS, AR, and WAWS methods are plotted in Figure 5. The blue and red curves are target and simulated PSD, respectively. As seen from Figure 5, the simulated results by the MS method are more accurate and closer to the target results. The numerical accuracy by the AR method in the lower and higher regions is the lowest compared to those by the MS and WAWS methods. Table 2 conducts further numerical accuracy analyses by the energy comparisons between the simulated and theoretical results using the MS, WAWS, and AR methods. Obviously, the error of the MS method is much lower than the others under the same initial conditions as 2.36% versus 7.21% and 11.94%.

These comparisons demonstrate that the MS method is a more accurate simulation method to generate the random loads compared to the WAWS and AR methods.

(2) *Validation for the Efficiency of the MS Method.* In general, a numerical wind tunnel needs the time series of the fluctuating

TABLE 3: The comparison of the computing time and accuracy at 36 and 108 spatial points using the MS, WAWS, and AR methods.

Number of nodes	Method	Error	Computing time (s)
	WAWS in MS	2.34%	256
36	AR in MS	6.24%	75
	MS	4.79%	331
	WAWS	4.24%	27465
	AR	22.96%	75
	WAWS in MS	2.07%	6766
108	AR in MS	9.40%	489
	MS	4.85%	7255
	WAWS	4.24%	647836
	AR	32.85%	489

wind of numerous spatial points rather than one single point. Time cost in computation becomes an important consideration in the numerical examples. The comparisons of the simulating time using the MS, WAWS, and AR methods, respectively, are carried out under the same computing conditions mentioned in Validation for the Accuracy of the MS Method.

The fluctuating wind velocities of 36 and 108 adjacent grid nodes in the inlet boundary sketched in Figure 3 are simulated by three abovementioned simulation methods. Table 3 gives a series of comparisons of computing time and accuracy of generating the fluctuating wind velocities at 36 and 108 adjacent spatial points using three simulation methods.

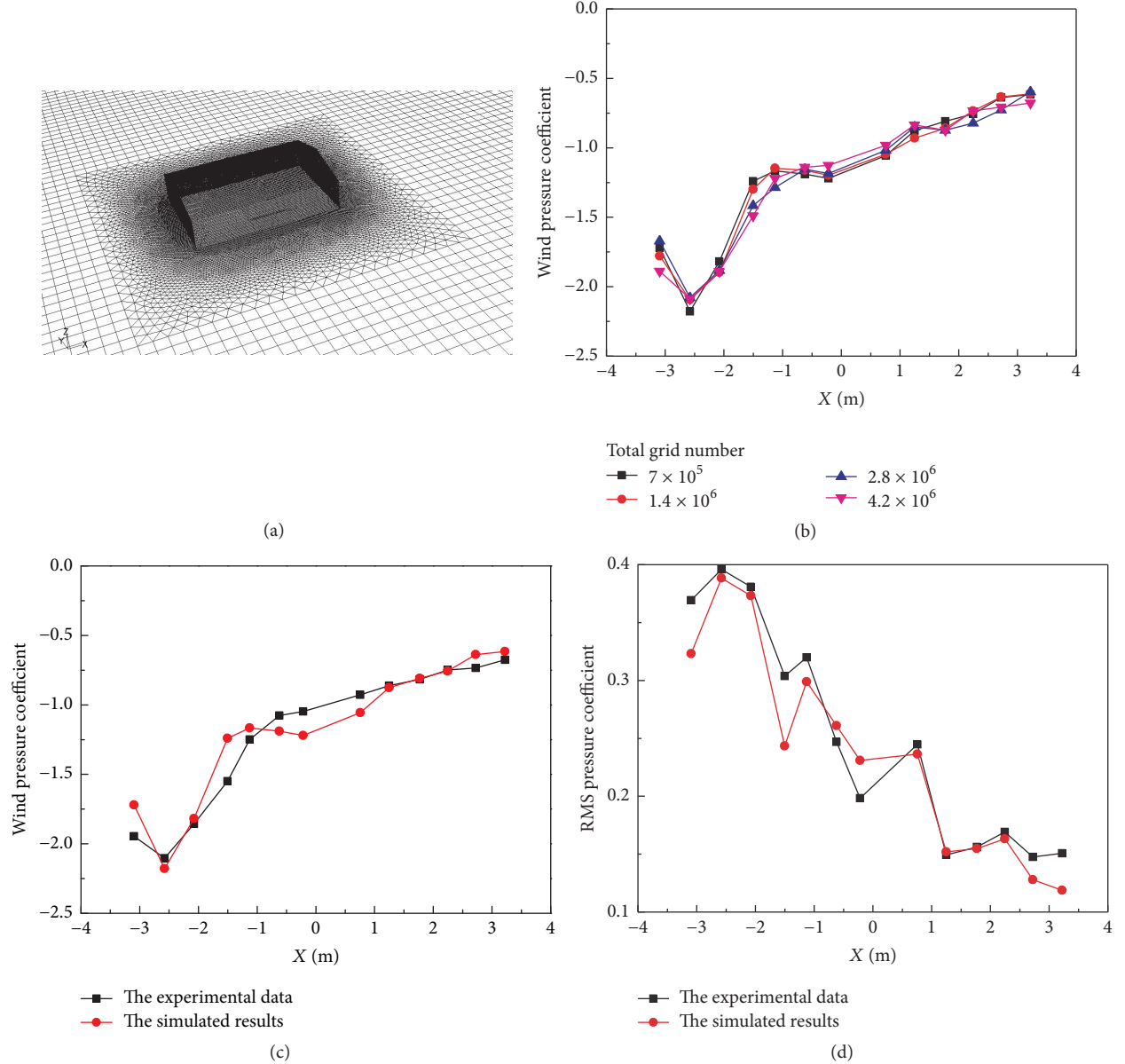


FIGURE 6: (a) The sketch of flow field and FB16 model. (b) Mesh independent tests. (c) The comparison of the wind pressure coefficients between the simulated and experimental results [21] of the roof on the windward side. (d) The comparison of the RMS wind pressure coefficients between the simulated and experimental results [21] of the roof on the windward side.

In Table 3, it is obvious to see that the increasing number of the spatial points could raise the computing difficulty including the computing time and accuracy. Although the calculating time by the AR method is always the shortest, the computing error increases rapidly from 11.94% of one single point to 32.85%. The simulating accuracy of the WAWS method is acceptable all the time, but time cost in computation of the WAWS method is nearly 100 times more than those of the MS method. Therefore, it is concluded that the MS method is a more efficient simulation method compared to the WAWS and AR methods.

Based on the two abovementioned validation tests, the MS method is an efficient and accurate simulation method integrating the advantages of the WAWS and AR methods.

6.1.2. Validation for the Method of CFD Numerical Wind Tunnel.

In order to validate the abovementioned CFD methods in Section 3 quickly, CFD predictions of FB16 in Figure 6(a) [21], whose dimensions are smaller than those of the offshore platform, are conducted as an initial solution of LES simulations. The computational treatment and algorithm are similar to Section 3. The dimensions of FB16 model are 12 m \times 6.7 m \times 5.3 m. The dimensions of the computational domain are defined as 420 m \times 55 m \times 15 m [12] and the blocking rate of the calculating model is less than 3%. The flow field and FB16 are sketched in Figure 6(a).

Through a series of mesh independent tests with the total grid number of 7.0×10^5 , 1.4×10^6 , 2.8×10^6 , and 4.2×10^6 , the wind coefficients of the roof on the windward side

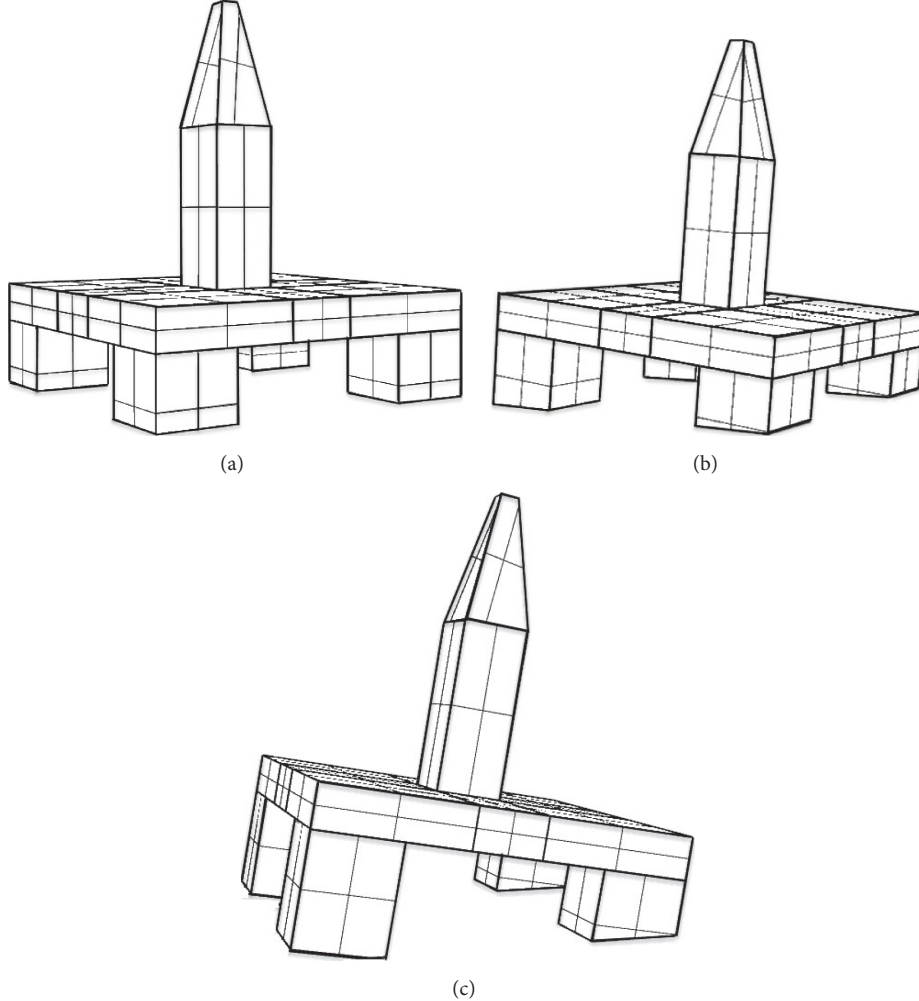


FIGURE 7: The sketch of the calculating model with three inclined angles: (a) 0° , (b) 5° , and (c) 10° .

are displayed in Figure 6(b). Since the total grid number increases from 7.0×10^5 to 4.2×10^6 , the wind coefficients have little change in value. For obtaining relative accuracies of the wind pressures, forces, and comparing wind coefficients, it is found that the present mesh in the present grid resolution test (i.e., the total grid number 7.0×10^5) can have a balance on time cost and numerical accuracy, which can satisfy the engineering requirements by and large. Therefore, the total grid number 7.0×10^5 is adopted in consideration of saving computing time while providing accurate results.

Figures 6(c) and 6(d) describe the numerical results and experimental data of the wind pressure coefficients and RMS pressure coefficients. Meanwhile, the red line represents the present CFD results and the dark line is extracted as the experimental data from [21]. The comparison shows that the trends of the curves are roughly in agreement and the maximum errors of wind pressure coefficient and RMS wind pressure coefficient between the numerical and experimental results are, respectively, less than 15% and 21%. Therefore, the LES method with these standards is available to carry out the following numerical examples.

6.2. Numerical Examples. In this section, attention is fixed on the wind field analyses of the offshore structures over the water as plotted in Figure 1 under the action of the harsh fluctuating wind. CFD numerical wind tunnel tests and wind-induced structural response analyses are presented in the following numerical studies.

6.2.1. CFD Wind Tunnel Predictions. The present work in this subsection is to analyze the wind pressure distributions and wind resultant forces of this platform with the inclined angles of 0° , 5° , and 10° plotted in Figure 7 at different wind directions. As the symmetry of the platform, 7 wind directions are defined within the range of 0° and 90° with intervals of 15° . Similar to the mesh independent simulations in the validation tests, the total grid number in the present LES simulations is approximately 1.1×10^7 .

According to [10, 20, 30], CFD simulations adopt the wind speed updating method by the joint application of MATLAB and Fluent. The wind speeds of the grid nodes in the inlet boundary are simulated by the MS method mentioned in Section 3 using self-compiled MATLAB codes. Using the

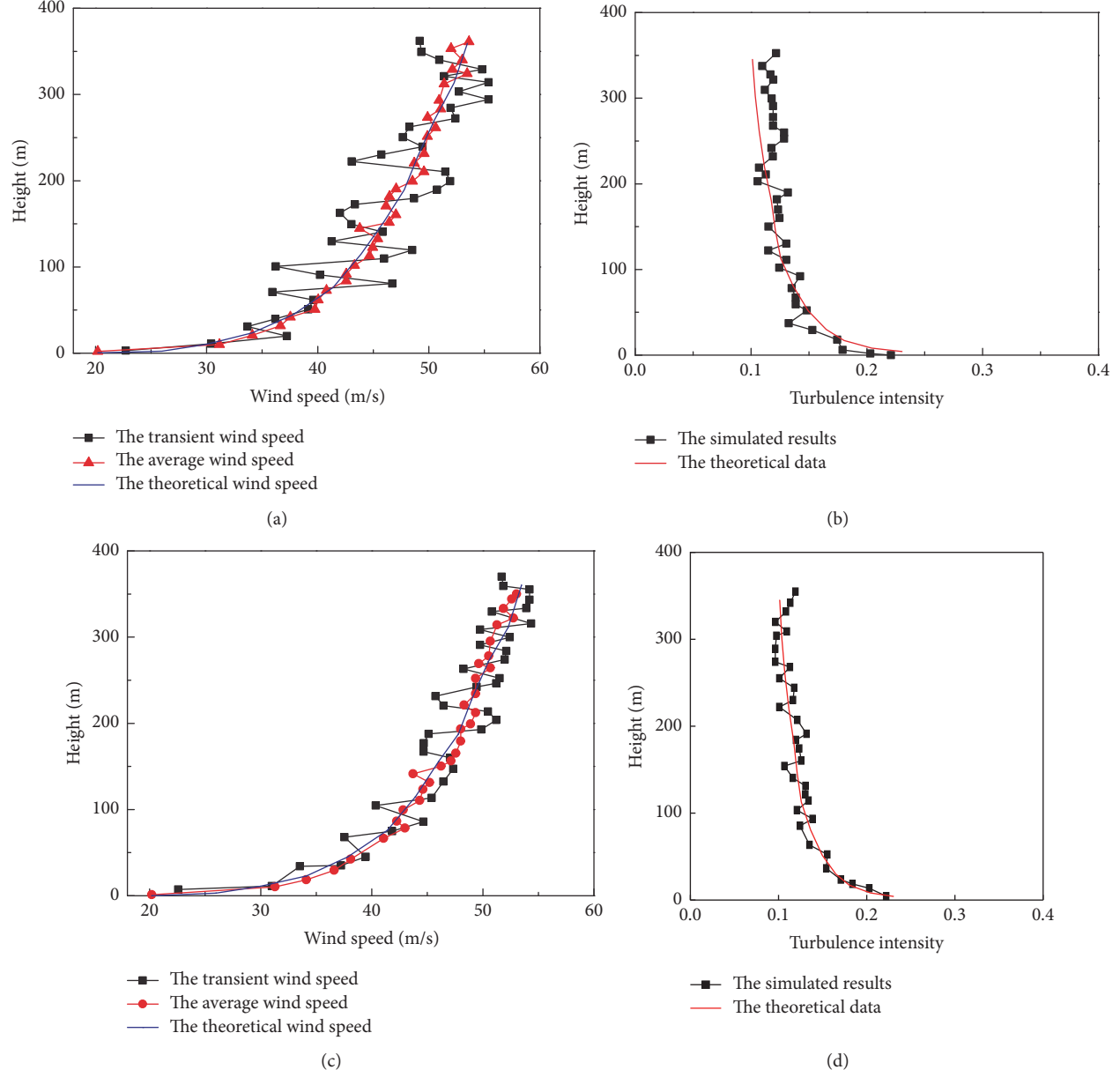


FIGURE 8: (a) Boundary layer profile at 1st time step at the inlet obtained to simulate the NPD profile [22]. (b) Turbulence intensity measurements at 1st time step at the inlet for NPD profile [22]. (c) Boundary layer profile at 100th time step at 100 m in front of the CFD numerical model obtained to simulate the NPD profile [22]. (d) Turbulence intensity measurements at 100th time step at 100 m in front of the CFD numerical model for NPD profile [22].

function of UDF, the velocity inlet conditions based on (3) and (5) are imported through the CFD interfaces into Fluent software, as sketched in Figure 3. Figure 8 gives the comparisons of the simulated and theoretical results of NPD wind profile and turbulence intensity [22] to validate whether the simulated results are in accordance with theoretical data to guarantee the numerical accuracy of CFD simulations. Among them, Figures 8(a) and 8(c) represent the wind profile comparisons at 1st time step at the inlet and at 100th time step at 100 m in front of the CFD numerical model, respectively. Figures 8(b) and 8(d) show the turbulence intensity comparisons at 1st time step at the inlet and at 100th time step

at 100 m in front of the CFD numerical model, respectively. The simulated results of wind profile and turbulence intensity are relatively in agreement with the theoretical data. The simulated results of the average wind speed and turbulence intensity are especially very close to the target values. Furthermore, the simulated results at 100th time step at 100 m in front of the CFD numerical model are relatively more accurate than those at 1st time step at the inlet by wind speed updating procedure in Section 3.1.4.

Figure 9(a) defines 2 lines used for demonstrating the accuracy of numerical simulation compared to existing experimental data and exploring some differences of wind

pressure distributions in different areas on the derrick (Figures 9(b) and 9(c)). Figures 9(b) and 9(c) plot the wind pressure distributions of two measuring lines on the windward side at 0° and 30° wind directions. Wind pressure decreases with a maximum of nearly 60% as the height increases. The curves of the present study are relatively close to those of the experimental results. The statistical results show the maximum differences of the wind coefficients at 0° and 30° wind directions between the numerical results and experimental data are, respectively, about 12.7% and 23.6%, which provides potentially acceptable results for engineering purpose. As seen from Figures 9(d) and 9(e), the simulated RMS wind coefficient curves in Line 1 are closer to the experimental curves than those in Line 2, whose curve trends are also in relative agreement with experimental curves. The maximum RMS wind coefficient errors at 0° and 30° wind directions in Line 1 are 23.2% and 23.9% and those in Line 2 are relatively larger, but less than 30%. Furthermore, the errors are speculated to be caused by the limited grid number and computational algorithm.

Figure 10 plots the shape coefficient and resultant wind forces of the platform over the water in 7 wind directions calculated by using the UDF function. Considering that the wind area of each local component of this platform changes at different wind directions, the variation of the shape coefficient is irregular in Figure 10(a). The shape coefficients of the derrick and deck reach their maximum at 0° wind direction (i.e., 1.50, 1.29, and 1.17), and the shape coefficient of the column is relatively large at 30° and 60° wind direction (i.e., 0.92 and 0.96). The curve trends of the numerical and experimental studies [18, 19] are relatively in good agreement. The numerical results are slightly smaller than the wind tunnel data and the errors between them are approximately 7.4% or less.

As seen from Figure 10(b), the curves of the wind forces in the horizontal position and inclination have the same trend. The wind loads of the flat and aslant platforms all increase from 0° to 45° wind direction and decrease from 45° to 90° wind direction. The maximum wind load appears at 45° wind direction in three positions of the platform which is in agreement with the experimental results [18, 19]. According to China Classification Society common rule and [19], the resultant wind forces are related to the windward area of the structural member, the wind speed, and pressure. The windward area of the aslant platform is larger than that of the flat platform. Therefore, the wind loads are increasing with the increasing inclined angles. The wind load takes the maximum value under the state of 45° wind direction and 10° inclined angle which is the most adverse survival state and the error between the simulated and experimental maximum resultant wind forces is about 4.8%: 16563 kN versus 17400 kN [18, 19].

6.2.2. The Wind-Induced Response Analyses. In light of the fact that the maximum wind resultant force appears at 45° wind direction and 10° inclined angle in the above subsection, the wind-induced structural responses of local components under this working condition are investigated in time domain by APDL.

Time series of the wind pressure at the top of the derrick and the statistics of wind pressures at different heights along Line 1 shown in Figure 9(a) are displayed in Figure 11. Thus, it can be seen that wind pressure decreases with the increasing height which matches the analyzed results in the LES predictions. Meanwhile, the change ranges of the mean and intermediate values are relatively larger than the other two values.

The wind-induced deformations at the top of the derrick at 45° wind direction are plotted in Figure 12. The displacements in x and y directions are relatively ten times larger than the deformation in the z direction. Due to conducting the wind-induced analysis at 45° wind direction, the displacements in the x and y directions are quite close listed as follows: the maximum displacements in the x and y directions are, respectively, 0.0028 m and 0.0034 m; the average displacements in two directions are both nearly 9.5×10^{-4} m. The displacement-time curves in three directions change stably around the average values.

The stress distributions of the local structures are displayed in Figure 13. It is found that the stresses at the top of the derrick and the connections between the derrick and deck at 45° wind direction are the largest which reaches 174 MPa. According to the current standards for building and classing offshore platforms formulated by China Classification Society, the maximum stress value is lower than the allowable stress of 345 MPa. It is demonstrated that the derrick could work well under this survival condition.

7. Conclusion

This paper mainly carries out the numerical simulations of the fluctuating wind effects and wind-induced response of a derrick on a semisubmersible platform by combining CFD and structural finite element analysis techniques. The computing results lead to the following conclusions.

(a) In the first validation test, the MS method is developed into an efficient and accurate simulation method which integrates the advantages of the WAWS and AR methods. Compared to the two traditional methods, the MS method is more applicable to simulate the fluctuating wind speed of numerous spatial nodes in consideration of the time cost and accuracy in computation. Taking the FB16 model for an object in another validation test, the simulated results are relatively close to the existing experimental data which demonstrated that LES methods are applicable in analyzing wind effects on a derrick.

(b) The curves of wind pressure and RMS pressure coefficients in the present study are relatively close to those in the experimental data. The errors of the pressure and RMS pressure coefficients, 10~30%, are relatively acceptable in consideration of computational efficiency and computer performances. The numerical shape coefficients are slightly smaller than the wind tunnel results overall and the errors between them are about 7.4% or less.

(c) In accordance with the existing experimental results, wind pressures decrease with a maximum of 60% as the height increases. The worst survival state in LES simulations and following dynamic response analyses occurs when the

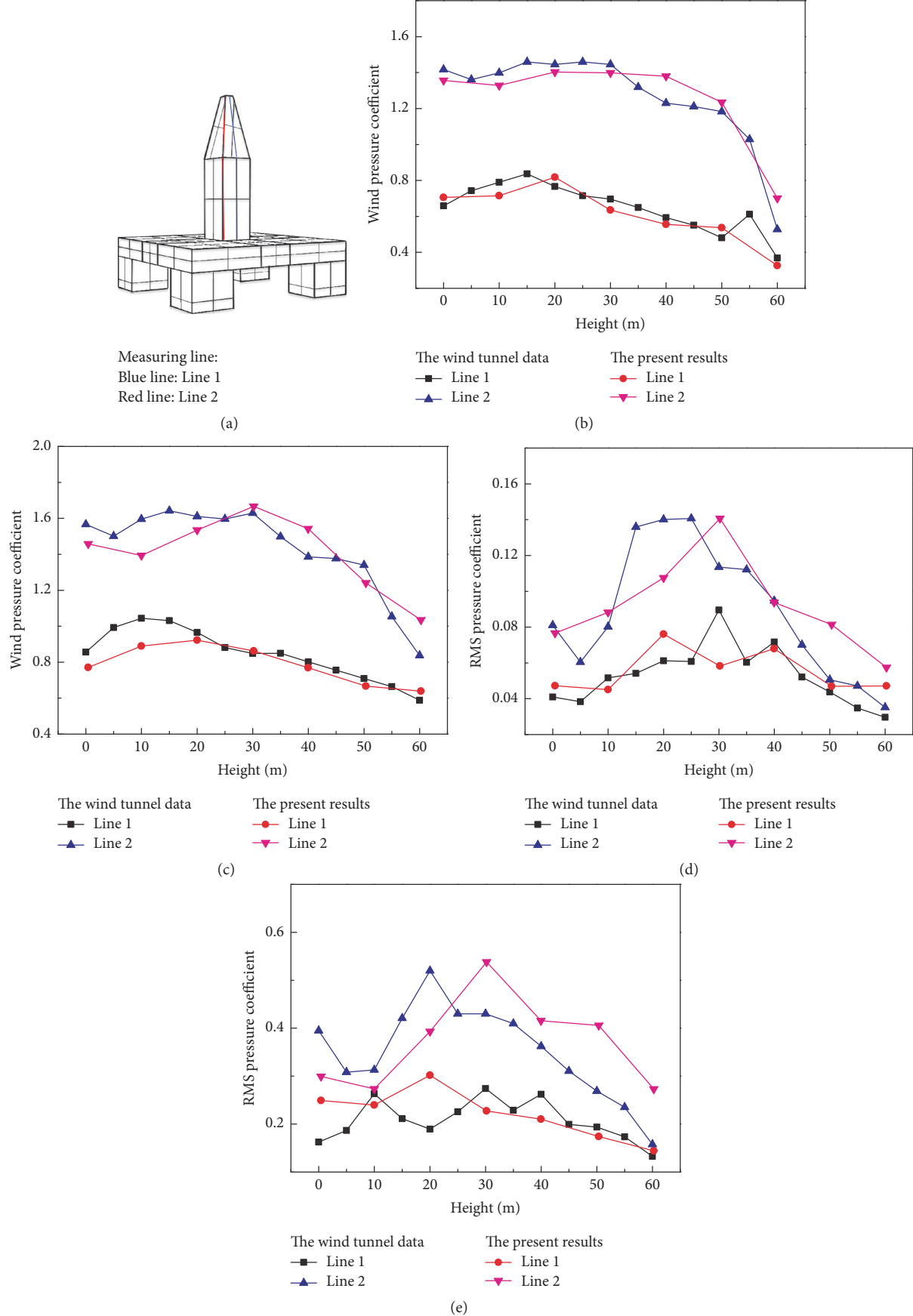


FIGURE 9: (a) Measuring line position. (b) Wind pressure coefficient of these lines on the windward side at 0° wind direction. (c) Wind pressure coefficient of these lines on the windward side at 30° wind direction. (d) RMS wind pressure coefficient of these lines on the windward side at 0° wind direction. (e) RMS wind pressure coefficient of these lines on the windward side at 30° wind direction.

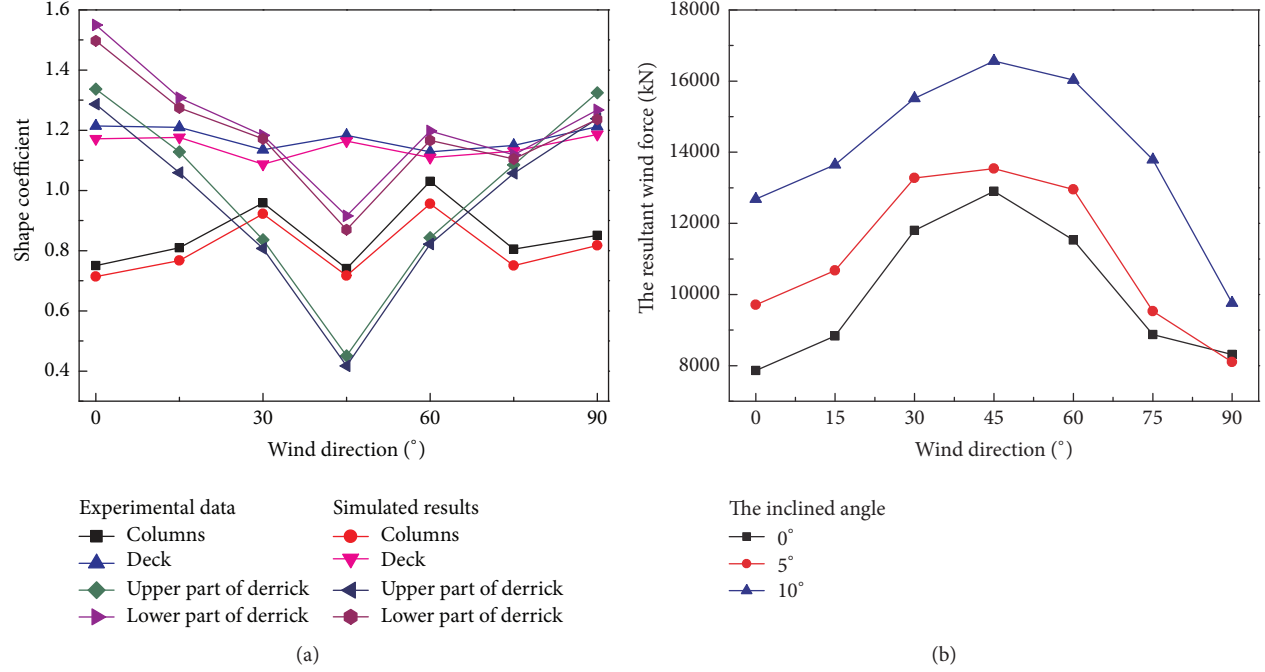


FIGURE 10: (a) The statistical shape coefficients of local components of the platform at different wind directions. (b) The statistical resultant wind forces of the platform over the water under different survival conditions.

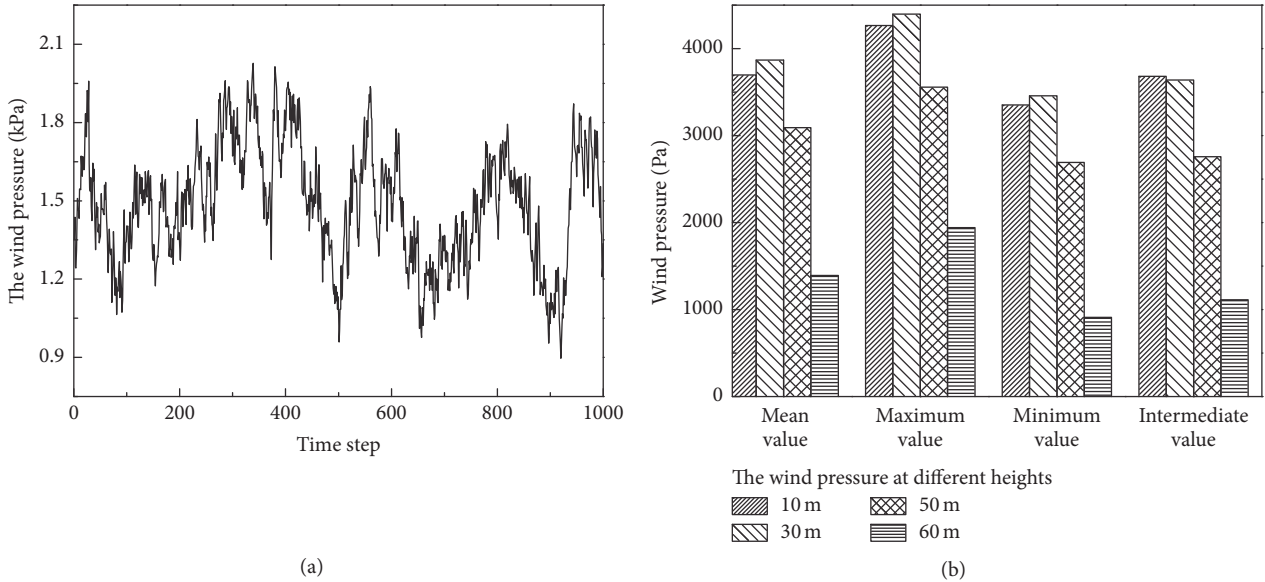


FIGURE 11: (a) The time series of the extracted wind pressure at the top of the derrick. (b) The wind pressure statistics of measuring points with different heights along Line 1.

wind resultant force reaches a maximum at 45° wind direction and 10° inclined angle.

(d) The wind-induced dynamic responses are calculated by the joint application of ANSYS Fluent and APDL. The displacements in three directions have certain periodicity and change steadily around the average value. The stresses at the

top of the derrick and the connections between the deck and derrick are the largest which is lower than the allowable stress. It is demonstrated that the offshore deck structures could work well in the worst survival condition.

In future works, the relationship between the wind scale, structural strength, and deformations could be investigated

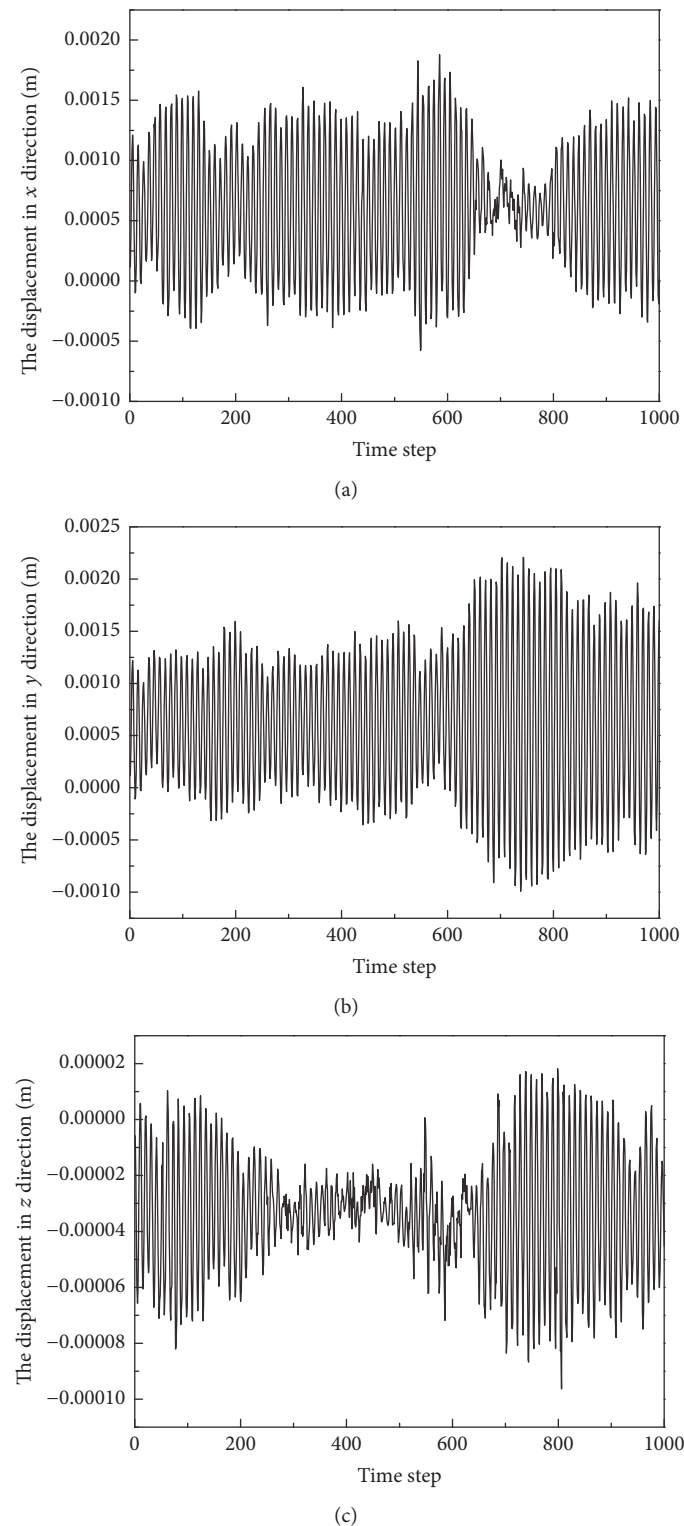


FIGURE 12: The displacement-time curves in three directions: (a) x direction, (b) y direction, and (c) z direction.

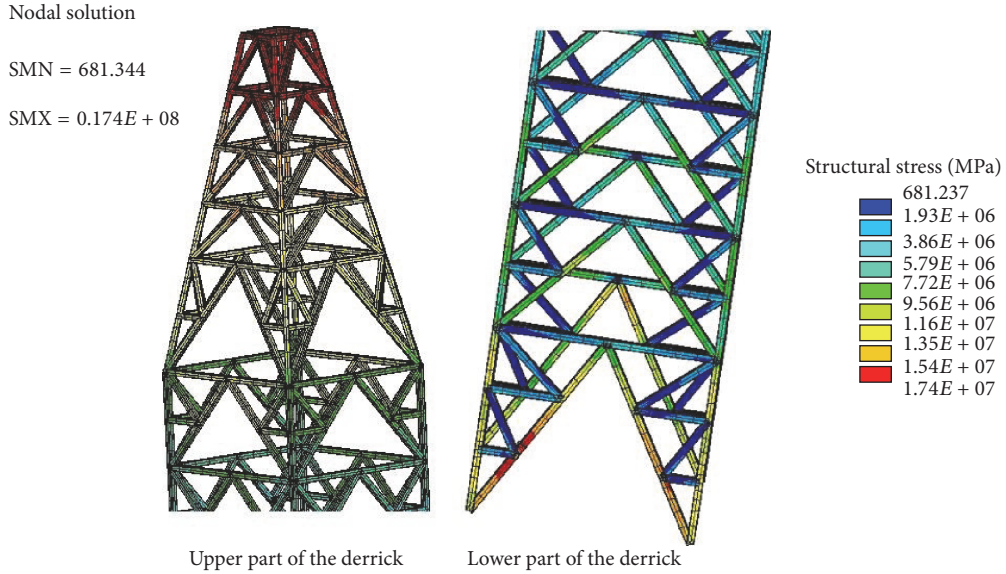


FIGURE 13: The stresses of the local structures of the derrick at 45° wind direction.

further. In addition, the effects of wind alone, wave alone, and the combined actions of both wind and wave on the offshore platform could be explored and compared.

Conflicts of Interest

The authors declare that there are no conflicts of interest regarding the publication of this paper.

Acknowledgments

Supports from National Natural Science Foundation of China (nos. 51679139, 51278297), the Major Program of the National Natural Science Foundation of China (no. 51490674), Research Program of Shanghai Leader Talent (no. 20), and Doctoral Disciplinary Special Research Project of Chinese Ministry of Education (no. 20130073110096) are acknowledged.

References

- [1] E. Shehata and A. Raheem, "Nonlinear behaviour of steel fixed offshore platform under environmental loads," *Ship and Offshore Structures*, vol. 11, no. 1, pp. 1–15, 2014.
- [2] A. A. Elshafey, M. R. Haddara, and H. Marzouk, "Dynamic response of offshore jacket structures under random loads," *Marine Structures*, vol. 22, no. 3, pp. 504–521, 2009.
- [3] S. Gomathinayagam, C. P. Vendhan, and J. Shanmugasundaram, "Dynamic effects of wind loads on offshore deck structures—a critical evaluation of provisions and practices," *Journal of Wind Engineering and Industrial Aerodynamics*, vol. 84, no. 3, pp. 345–367, 2000.
- [4] J. Jia, "Investigations of a practical wind-induced fatigue calculation based on nonlinear time domain dynamic analysis and a full wind-directional scatter diagram," *Ships and Offshore Structures*, vol. 9, no. 3, pp. 272–296, 2014.
- [5] M. I. Kvitem and T. Moan, "Frequency versus time domain fatigue analysis of a semi-submersible wind turbine tower," *Journal of Offshore Mechanics and Arctic Engineering*, vol. 137, no. 1, Article ID 011901, 2015.
- [6] K. Wang, T. Moan, and M. O. L. Hansen, "Stochastic dynamic response analysis of a floating vertical-axis wind turbine with a semi-submersible floater," *Wind Energy*, vol. 19, no. 10, pp. 1853–1870, 2016.
- [7] C. J. Lu, S. N. Lu, and X. D. Wang, "Wind-induced dynamic analysis of the arched tensegrity structures in time domain," *Computing in Civil and Building Engineering*, vol. 166–169, pp. 140–143, 2014.
- [8] C. J. Baker, "Wind engineering—past, present and future," *Journal of Wind Engineering and Industrial Aerodynamics*, vol. 95, no. 9–11, pp. 843–870, 2007.
- [9] Q. S. Li, J. R. Wu, S. G. Liang, Y. Q. Xiao, and C. K. Wong, "Full-scale measurements and numerical evaluation of wind-induced vibration of a 63-story reinforced concrete tall building," *Engineering Structures*, vol. 26, no. 12, pp. 1779–1794, 2004.
- [10] C. L. Lu, Q. S. Li, S. H. Huang, F. B. Chen, and X. Y. Fu, "Large eddy simulation of wind effects on a long-span complex roof structure," *Journal of Wind Engineering and Industrial Aerodynamics*, vol. 100, no. 1, pp. 1–18, 2012.
- [11] G. Diana, D. Rocchi, and M. Belloli, "Wind tunnel: a fundamental tool for long-span bridge design," *Structure and Infrastructure Engineering*, vol. 11, no. 4, pp. 533–555, 2015.
- [12] B. Yan and Q. Li, "Large-eddy simulation of wind effects on a super-tall building in urban environment conditions," *Structure and Infrastructure Engineering*, vol. 12, no. 6, pp. 765–785, 2016.
- [13] S. Huang, Q. S. Li, and S. Xu, "Numerical evaluation of wind effects on a tall steel building by CFD," *Journal of Constructional Steel Research*, vol. 63, no. 5, pp. 612–627, 2007.
- [14] M. J. Muliawan, M. Karimirad, and T. Moan, "Dynamic response and power performance of a combined Spar-type floating wind turbine and coaxial floating wave energy converter," *Renewable Energy*, vol. 50, no. 3, pp. 47–57, 2013.
- [15] J. Chen, R. Yang, and R. Ma, "Wind field simulation of large horizontal-axis wind turbine system under different operating

- conditions," *Structural Design of Tall and Special Buildings*, vol. 24, no. 17, pp. 973–988, 2015.
- [16] C. C. Zang, J. M. Christian, J. K. Yuan et al., "Numerical simulation of wind loads and wind induced dynamic response of heliostats," *Energy Procedia*, vol. 49, pp. 1582–1591, 2013.
- [17] D. Hill, K. R. Bell, D. McMillan, and D. Infield, "A vector auto-regressive model for onshore and offshore wind synthesis incorporating meteorological model information," *Advances in Science and Research*, vol. 11, pp. 35–39, 2014.
- [18] G. Zhai, Z. Ma, and H. Zhu, "The wind tunnel tests of wind pressure acting on the derrick of deepwater semi-submersible drilling platform," in *Proceedings of the 2011 2nd International Conference on Advances in Energy Engineering (ICAEE '11)*, vol. 14, pp. 1267–1272, Bangkok, Thailand, December 2011.
- [19] H. Zhu, Z. Ma, G. J. Zhai, B. Xie, Y. J. Fu, and J. P. Ou, "Numerical simulation and wind tunnel tests of wind loads acting on HYSY-981 semi-submersible platform," *Ship & Ocean Engineering*, vol. 38, no. 5, pp. 149–152, 2009 (Chinese).
- [20] D. Lu, C. M. Li, and G. J. Wang, "CFD unsteady state numerical simulation of wind-induced vibration of the Shanghai Jinmao building," *China Civil Engineering Journal*, vol. 41, no. 8, pp. 31–35, 2008 (Chinese).
- [21] R. P. Hoxey and A. P. Robertson, "Pressure coefficients for low-rise building envelopes derived from full-scale experiments," *Journal of Wind Engineering and Industrial Aerodynamics*, vol. 53, no. 1-2, pp. 283–297, 1994.
- [22] A. J. Coulling, A. J. Goupee, A. N. Robertson, J. M. Jonkman, and H. J. Dagher, "Validation of a FAST semi-submersible floating wind turbine numerical model with DeepCwind test data," *Journal of Renewable and Sustainable Energy*, vol. 5, no. 2, Article ID 023116, 2013.
- [23] ANSYS Inc, *ANSYS FLUENT Tutorial Guide*, ANSYS Inc, Canonsburg, Pa, USA, 2012.
- [24] Y. Quan, S. Wang, M. Gu, and J. Kuang, "Field measurement of wind speeds and wind-induced responses atop the shanghai world financial center under normal climate conditions," *Mathematical Problems in Engineering*, vol. 2013, Article ID 902643, 14 pages, 2013.
- [25] B. W. Yan and Q. S. Li, "Inflow turbulence generation methods with large eddy simulation for wind effects on tall buildings," *Computers and Fluids*, vol. 116, pp. 158–175, 2015.
- [26] S. Huang and Q. S. Li, "A new dynamic one-equation subgrid-scale model for large eddy simulations," *International Journal for Numerical Methods in Engineering*, vol. 81, no. 7, pp. 835–865, 2010.
- [27] T. Kajishima and T. Nomachi, "One-equation subgrid scale model using dynamic procedure for the energy production," *Journal of Applied Mechanics, Transactions ASME*, vol. 73, no. 3, pp. 368–373, 2006.
- [28] M. Okamoto and N. Shima, "Investigation for the one-equation-type subgrid model with eddy-viscosity expression including the shear-dumping effect," *JSME International Journal, Series B: Fluids and Thermal Engineering*, vol. 42, no. 2, pp. 154–161, 1999.
- [29] C. Peyrard, M. Belloli, P. Bousseau et al., "CFD modeling of flow induced vibration on a mobile cylinder fro a 30 k–60 k Reynolds number comparison between simulation and experimental results," in *Proceedings of the ASME 2009 Pressure Vessels and Piping Division Conference (PVP '09)*, pp. 301–308, Prague, Czech Republic, July 2009.
- [30] E. Shirani, J. H. Ferziger, and W. C. Reynolds, "Mixing of a passive scalar in isotropic and sheared homogeneous turbulence," NASA STI/Recon Technical Report N TF-15, 1981.
- [31] J. Hu and J. Wang, "Short-term wind speed prediction using empirical wavelet transform and Gaussian process regression," *Energy*, vol. 93, pp. 1456–1466, 2015.
- [32] H. Liu, H.-Q. Tian, D.-F. Pan, and Y.-F. Li, "Forecasting models for wind speed using wavelet, wavelet packet, time series and Artificial Neural Networks," *Applied Energy*, vol. 107, pp. 191–208, 2013.
- [33] W. Cui, L. Liu, X. Yang, Y. Wang, L. Feng, and V. Springel, "An ideal mass assignment scheme for measuring the power spectrum with fast fourier transforms," *Astrophysical Journal*, vol. 687, no. 2, pp. 738–744, 2008.
- [34] J. Ma, *The research of wind field and fluid-structure-interaction and fine identification for space structure [Ph.D. thesis]*, Shanghai Jiao Tong University, 2008.
- [35] A. Testa, D. Gallo, and R. Langella, "On the processing of harmonics and interharmonics: using hanning window in standard framework," *IEEE Transactions on Power Delivery*, vol. 19, no. 1, pp. 28–34, 2004.
- [36] J. Nunn, L. J. Wright, C. Söller, L. Zhang, I. A. Walmsley, and B. J. Smith, "Large-alphabet time-frequency entangled quantum key distribution by means of time-to-frequency conversion," *Optics Express*, vol. 21, no. 13, pp. 15959–15973, 2013.
- [37] Y.-H. Liu, Q. H. Liu, and Z.-P. Nie, "A new efficient FDTD time-to-frequency-domain conversion algorithm," *Progress in Electromagnetics Research*, vol. 92, pp. 33–46, 2009.

